catalysts

MDPI

Communication

Magnetically Separable Mixed-Phase α/γ-Fe_2O_3 Catalyst for Photo-Fenton-like Oxidation of Rhodamine B

Asiyat Magomedova [1], Abdulgalim Isaev [1,*], Farid Orudzhev [1], Dinara Sobola [1,2,3], Rabadanov Murtazali [1], Alina Rabadanova [1], Nabi S. Shabanov [4], Mingshan Zhu [5], Ruslan Emirov [1], Sultanakhmed Gadzhimagomedov [1], Nariman Alikhanov [1] and Kaviyarasu Kasinathan [6,7]

1 Department of Inorganic Chemistry and Chemical Ecology, Dagestan State University, St. M. Gadjieva 43-a, 367015 Makhachkala, Russia; asiyat_magomedova1996@mail.ru (A.M.); farid-stkha@mail.ru (F.O.); sobola@vut.cz (D.S.); rab_mur@mail.ru (R.M.); aderron@mail.ru (R.E.); darkusch@mail.ru (S.G.); alihanov.nariman@mail.ru (N.A.)
2 Department of Physics, Faculty of Electrical Engineering and Communication, Brno University of Technology, Technická 2848/8, 61600 Brno, Czech Republic
3 Central European Institute of Technology BUT, Purkyňova 123, 61200 Brno, Czech Republic
4 Dagestan Federal Research Centre of the Russian Academy of Sciences, Analytical Center for Collective Use, M. Gadjieva 45, 367001 Makhachkala, Russia; shabanov.nabi@yandex.ru
5 School of Environment, Jinan University, Guangzhou 511443, China; zhumingshan@jnu.edu.cn
6 UNESCO-UNISA Africa Chair in Nanoscience's/Nanotechnology Laboratories, College of Graduate Studies, University of South Africa (UNISA), Muckleneuk Ridge, Pretoria P.O. Box 392, South Africa; kasinathankaviyarasu@gmail.com
7 Nanosciences African Network (NANOAFNET), Materials Research Group (MRG), iThemba LABS-National Research Foundation (NRF), 1 Old Faure Road Western Cape Province, Cape Town P.O. Box 722, South Africa
* Correspondence: abdul-77@yandex.ru; Tel.: +7-963-427-97-78

check for updates

Citation: Magomedova, A.; Isaev, A.; Orudzhev, F.; Sobola, D.; Murtazali, R.; Rabadanova, A.; Shabanov, N.S.; Zhu, M.; Emirov, R.; Gadzhimagomedov, S.; et al. Magnetically Separable Mixed-Phase α/γ-Fe_2O_3 Catalyst for Photo-Fenton-like Oxidation of Rhodamine B. *Catalysts* **2023**, *13*, 872. https://doi.org/10.3390/catal13050872

Academic Editors: Meng Li and Marta Pazos Currás

Received: 20 March 2023
Revised: 22 April 2023
Accepted: 8 May 2023
Published: 11 May 2023

Abstract: Iron oxides are widely used as catalysts for photo-Fenton-like processes for dye oxidation. In this study, we report on the synthesis of an α/γ-Fe_2O_3 mixed-phase catalyst with magnetic properties for efficient separation. The catalyst was synthesized using glycine–nitrate precursors. The synthesized α/γ-Fe_2O_3 samples were characterized using scanning electron microscopy, X-ray diffraction spectroscopy (XRD), Raman shift spectroscopy, X-ray photoelectron spectroscopy (XPS), and vibrating sample magnetometer (VSM). The diffraction peaks were indexed with two phases, α-Fe_2O_3 as the main phase (79.6 wt.%) and γ-Fe_2O_3 as the secondary phase (20.4 wt.%), determined using the Rietveld refinement method. The presence of Fe^{2+} was attributed to oxygen vacancies. The mixed-phase α/γ-Fe_2O_3 catalyst exhibited remarkable photo-Fenton-like degradation performance for Rhodamine B (RhB) in neutral pH. The effects of operating parameters, including H_2O_2 concentration, catalyst concentration, and RhB concentration, on the degradation efficiency were investigated. The removal rates of color were 99.2% after 12 min at optimal conditions of photo-Fenton-like oxidation of RhB. The sample exhibited a high saturation magnetization of 28.6 emu/g. Additionally, the α/γ-Fe_2O_3 mixed-phase catalyst showed long-term stability during recycle experiments, with only a 5% decrease in activity.

Keywords: iron oxides; α/γ-Fe_2O_3 mixed-phase catalyst; magnetically separable; Rhodamine B; photo-Fenton-like

1. Introduction

Advanced oxidation processes are currently being utilized as an effective method for treating industrial wastewater that contains non-biodegradable organic compounds [1]. One of the most extensively studied oxidation processes is the Fenton process, which utilizes hydrogen peroxide and ferrous ions and exhibits an effective ability to destroy a wide range of contaminants. However, this process can only be effectively used with acidic or neutral pH wastewater [2]. The Fenton process is a homogeneous catalytic system,

where the catalyst (Fe^{2+}) is added in the form of a soluble salt and is removed from the reactor with the outgoing stream of purified water, due to the impossibility of its separation. This problem is further exacerbated by the fact that upon further neutralization of the purified solution, Fe^{3+} precipitates, necessitating the separation of the resulting precipitate, which collectively leads to a decrease in the efficiency of the process [3]. In this regard, the use of the heterogeneous Fenton-like process in the presence of iron compounds in the form of a precipitate on which the hydroxyl radical is generated from hydrogen peroxide is more promising [4]. Heterogeneous Fenton-like reactions can also efficiently degrade organic compounds in wastewater [5,6]. Solid catalysts can be reused after separation [7,8]. The use of the heterogeneous Fenton-like process overcomes some of the disadvantages of the homogeneous Fenton reaction, such as reduced reactivity due to catalyst consumption and the need to adjust pH [9].

At the same time, it is known that in the dark processes of homogeneous and heterogeneous Fenton, Fe^{3+} ions accumulate in the system and the reaction rate decreases significantly with time and stops after the complete consumption of Fe^{2+} ions [10]. The combination of Fenton and Fenton-like processes with simultaneous exposure to UV/visible radiation ($\lambda < 600$ nm) can solve this problem due to the photoreduction reaction of Fe^{3+} ions to Fe^{2+} [11].

Iron oxides are among the widely used materials as catalysts for Fenton-like processes for the oxidation of organic compounds [12–16]. Among the most studied and promising iron oxides and hydroxides for use as catalysts in Fenton-like processes, magnetite (Fe_3O_4) [17–24], goethite (α-FeOOH) [25,26], maghemite (γ-Fe_2O_3) [12,27–31], and hematite (α-Fe_2O_3) [32–34] can be noted. Various physicochemical characteristics of these oxides make them more or less favorable for oxidative reactions. These solid catalysts have good potential to degrade bio-oxidation-resistant contaminants [35,36]. Among these crystal structures, hematite is the most stable state of iron oxide under environmental conditions [37]. The prevailing use of α-Fe_2O_3 is due to its excellent physical and chemical properties, which can manifest themselves in samples with different morphology [38–40], particle size [41], and also in composite structures [42–44], which is especially important for creation of efficient heterogeneous catalysts in Fenton-like oxidation processes [45,46]. Maghemite also finds use as a catalyst in Fenton-like processes for the oxidation of organic compounds [47,48]. Unlike α-Fe_2O_3, γ-Fe_2O_3 is magnetic and can be easily reduced using a magnet. At the same time, γ-Fe_2O_3 retains catalytic activity for many cycles of use [49].

Various methods are used to synthesize iron oxides [50]. Specifically, the solution combustion method, using glycine as a fuel, was employed to synthesize α-Fe_2O_3 and γ-Fe_2O_3 [51–53]. This method results in the formation of ultra-small α-Fe_2O_3 nanoparticles (less than 5 nm) that exhibit superparamagnetism in the temperature range of 70–300 K [54]. Additionally, biphasic α/γ-Fe_2O_3 nanoparticles have been reported, which demonstrate high sensitivity to detecting volatile organic compounds such as acetone [55] and ethanol [56]. Biphasic α/γ-Fe_2O_3 exhibits significantly higher sensitivity than α-Fe_2O_3 and γ-Fe_2O_3 alone [57]. The work [58] reports higher photocatalytic activity of heterophase α/γ-Fe_2O_3 during methylene blue oxidation due to a decrease in the rate of electron-hole pair recombination. Therefore, a new approach to enhance metal oxide catalyst performance is to integrate different crystalline forms of the same metal oxide into a single structure. Currently, there is no information available on the use of biphasic α/γ-Fe_2O_3 in Fenton-like processes for organic compound oxidation. Based on this, this paper investigates the production of biphasic iron oxide and its use as a magnetically separable heterogeneous catalyst in the Fenton-like process for RhB oxidation.

2. Results

2.1. Catalyst Characterizations

Iron oxides (Fe_2O_3) with various ratios of fuel and oxidizer (φ) were synthesized using the conventional solution combustion method. Glycine is widely used in the so-called glycine–nitrate synthesis of metal oxide nanoparticles by combustion [56,57].

The ongoing combustion reaction can be written according to Equation (1).

$$6Fe(NO_3)_3 + 10C_2H_5NO_2 \rightarrow 3Fe_2O_3 + 20CO_2 + 14N_2 + 25H_2O \quad (1)$$

The coefficients of the expected reaction were placed based on the theory of combustion [59]. The fuel–oxidizer ratio of 0.4 ($\varphi < 1$) was chosen so that the amount of oxidizer was in excess and there was no need for atmospheric oxygen. Additionally, it was shown that in several systems, solution combustion synthesis of reactive solutions with an excess of fuel ($\varphi > 1$) leads to the formation of pure metals [60].

The morphology of the synthesized powders was studied using SEM. The images at various magnifications are shown in Figure 1.

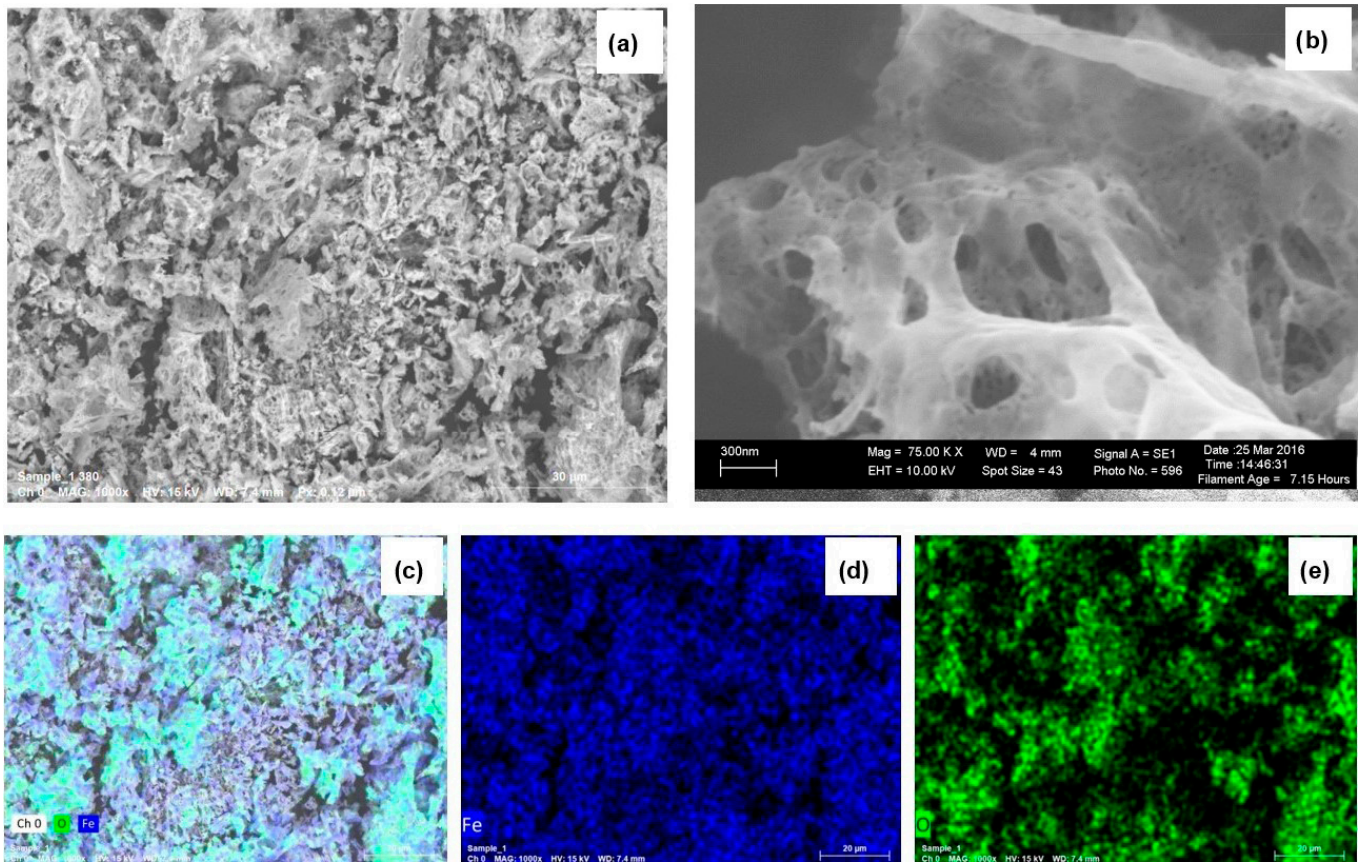

Figure 1. SEM images of catalyst samples at various magnifications (**a**,**b**). EDS elemental mapping of the selected area (**c**–**e**).

In Figure 1a, at low magnifications, it can be seen that the powder has a loose flaky texture characteristic of the combustion method with a large number of pores. At high magnifications in Figure 1b, one can see that the powder is in the form of large submicron agglomerates of a bone-like structure, sintered at high temperatures during synthesis. In this case, the grain boundaries are quite clearly traced. It can be seen that, along with large micron-sized pores, there is a large number of nanopores. From the EDS images (Figure 1c–e), it is clearly seen that the atoms of iron and oxygen are uniformly distributed over the surface under study. EDX spectra are presented in Supplementary Materials (Figure S1). Analysis of the atomic percentage of the elements Fe and O showed that the ratio is close to stoichiometric, Fe (47 wt.%) O (53 wt.%) with a slight oxygen deficiency.

It is known from the literature that varying the fuel-oxidizer ratio affects the phase of the synthesized iron oxide [61]. Therefore, the crystal structure of the powder was investigated by XRD and Raman methods. The data are presented in Figure 2a,b.

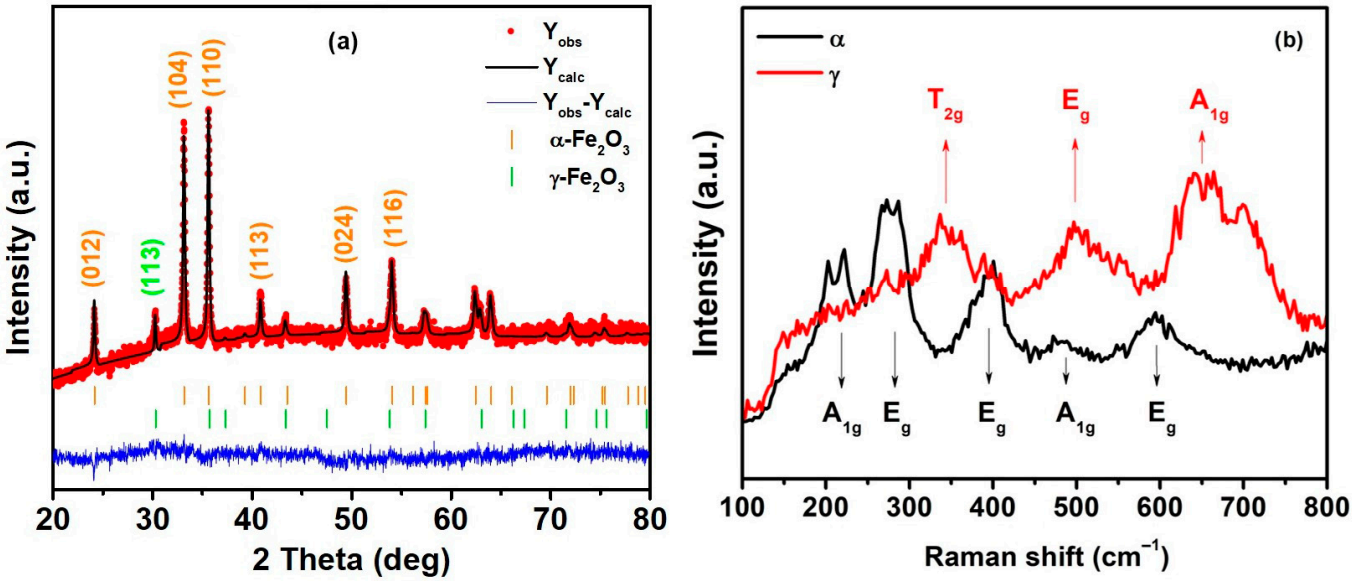

Figure 2. (**a**) Rietveld refinement graphs of Fe_2O_3. The red circles indicate the experimental data, the black line is the fitting value, the blue line is the difference, and the orange and green ticks are the Bragg reflections of the α-phase and γ-phase, respectively. (**b**) Raman spectra in different areas.

Figure 2a shows the XRD spectrum of the sample with the structure refined by the Rietveld method. The spectrum is well described by two phases, namely α-Fe_2O_3 with Hexagonal structure and space group R-3c (Ref. Code 98-006-6756) and γ-Fe_2O_3 with Cubic structure and space group Fd-3m (Ref. Code 98-006-6756). Quantitative phase evaluation carried out using the Rietveld method showed that α-Fe_2O_3 exists as the main phase (79.6 wt.%) and γ-Fe_2O_3 is present in an amount (20.4 wt.%). The presence of background noise indicates a high proportion of amorphous Fe_2O_3 in the sample. The Rietveld reliability factors displayed in Table 1 show that the quality of the fit is appreciable.

Table 1. Results of phase quantification and Rietveld refinement of Fe_2O_3.

		Sample	
Phases		α-Fe_2O_3	γ-Fe_2O_3
wt.%		79.6	20.4
Space group		R-3c (No. 167)	F d-3 m (No. 227)
Crystal system		Hexagonal	Cubic
Lattice parameters	a (Å)	5.0339	8.3421
	c (Å)	13.742	-
Cell volume	V (Å^3)	301.57	580.53
Rietveld reliability factors	R_{exp}	1.5628	
	R_w	1.7091	
	R_p	1.3556	
	GoF	1.1961	
Crystallite size	L_{Vol-IB} (nm)	47.4	45.7

The resulting fitted D-V function was then used for the calculation of volume-weighted mean crystallite size (L_{Vol-IB}) via the Scherrer equation. The average crystallite size of α-phase was found to be 47.4 nm, while that of the γ-phase was 45.7 nm.

Iron oxide polymorphs of the α- and γ-phases are also distinguishable by Raman spectroscopy. The Raman spectra from two different parts of the sample are shown in Figure 2b. The black line shows two classes of Raman active modes of hematite in the range from 200 to 800 cm^{-1}. The existence of characteristic A 1g bands at 221 and 491 cm^{-1} and Eg bands at 239, 287, 401, and 605 cm^{-1}, respectively, is attributed to the main hematite bands. Low-frequency modes (200–300 cm^{-1}) were attributed to vibrations of the Fe atom,

and bands from 400 to 650 cm^{-1} were attributed to vibrations of the O atom [62–65]. The red line in Figure 2b shows three Raman active phonon modes at 365 cm^{-1} (T2g), 511 cm^{-1} (Eg), and 700 cm^{-1} (A1g), characteristic of maghemite. The spectrum is in good agreement with the data for maghemite previously published in the literature [66–68].

The surface states play a key role for heterogeneous photo-Fenton-like catalysis; the surface was investigated by XPS. The obtained results are presented in Figure 3.

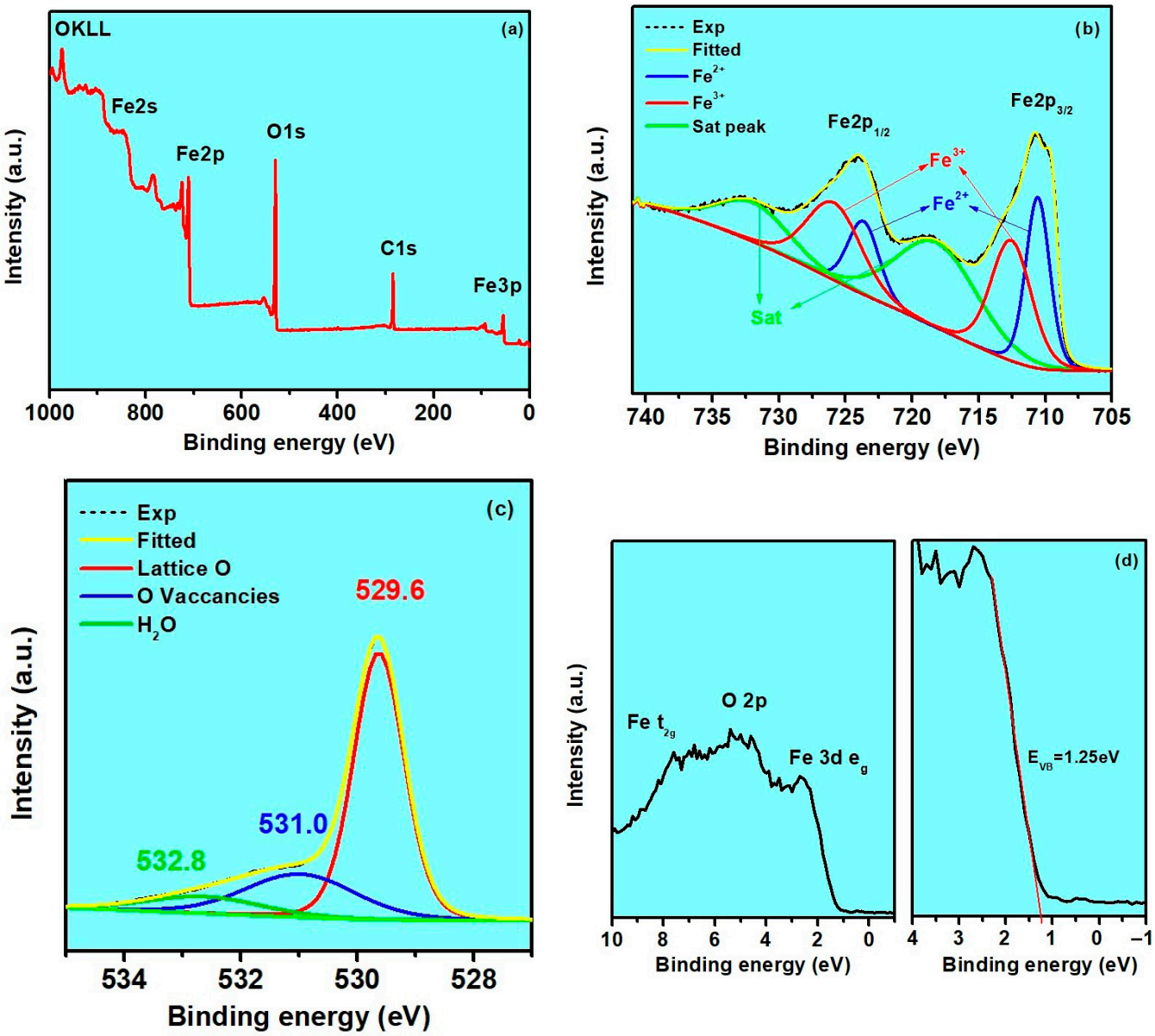

Figure 3. XPS spectra of as-prepared mixed-phase α/γ-Fe_2O_3 catalyst: full spectra (**a**); Fe 2p (**b**); O 1s (**c**); and Fe 3p (**d**) core-level spectra.

With a wide panoramic scan in Figure 3a, peaks of C 1s, O 1s, and Fe 2p were detected, which indicates the absence of impurities. Peak C 1s comes from random carbon [67,69,70]. The high-resolution spectrum of Fe 2p after deconvolution with approximation of Gaussian peaks is shown in Figure 3b. It can be seen that the spectrum is well described by the superposition of six peaks. There were two peaks at 726.1 and 712.5 eV, which are typical characteristic peaks of Fe^{3+} in 2p 1/2 and 2p 3/2 orbitals [71]. In addition, two deconvoluted peaks at 723.9 and 710.5 eV correspond to Fe^{2+}, which can be due both to the presence of magnetite in the structure, which is quite difficult to distinguish from maghemite by XRD

and Raman methods, and to the formation of oxygen vacancies in Fe_2O_3. Generation of oxygen vacancies in the crystal lattice leaves two electrons per missing oxygen atom, which leads to the reduction of Fe^{3+} to Fe^{2+} [72]. The generation of oxygen vacancies is common for the high-temperature combustion method [73]. The two deconvolution peaks at 732.1 and 718.3 eV are attributed to the presence of their satellite vibrational peaks (labeled "Sat."). From a comparison of the integral areas of the Fe^{3+} peaks in Fe^{2+}, it was found that their ratio is 60:40%. Data are presented in Supplementary Materials (Figures S2 and S3).

To confirm the presence of oxygen vacancies, the spectrum of the O 1s level was studied. Figure 3c shows the O 1s spectra after deconvolution with approximation of Gaussian peaks. The spectrum is well described by the superposition of three components centered at 529.6, 531.0, and 532.8 eV, respectively. The peak at 529.6 was a typical lattice oxygen peak, and that at 531.0 eV could be attributed to the low-coordinated oxygen species adsorbed onto the oxygen vacancies. The peak at 532.8 eV was assigned to the hydroxyl species of surface-adsorbed H_2O molecules [74].

The XPS results indicate the co-presence of Fe^{2+} and Fe^{3+} and that the presence of Fe^{2+} is not associated with the presence of magnetite in the structure, confirming the results of XRD and Raman. It is important that the Fe^{2+}/Fe^{3+} redox pair formed on the surface can accelerate the charge transfer in Fe_2O_3, since Fe^{3+} is reduced to Fe^{2+} during heterogeneous Fenton-like catalysis [75].

The XPS valence band (VB) region analysis is a powerful tool for understanding the electronic structure of a material. Figure 3d shows the XPS (VB) spectrum in the binding energy range 0–10 eV. The VB spectrum is the result of hybridization of Fe3d and O 2p atomic orbitals [76] and can apparently be described by three bands, which is consistent with previously published results [77] and corresponds to the states of Fe 3d eg strongly hybridized with O 2p and non-bonding O 2p, and the C characteristic is dominated by bond states of the O 2p and Fe t2g orbitals. The inset to Figure 3d shows that the valence band maximum (VBM) is 1.25 eV below the Fermi level.

2.2. Catalytic Activity in Fenton-like Process

The catalytic activity of two-phase α/γ-Fe_2O_3 was studied by oxidation of the dye RhB under various conditions. Figure 4 shows a typical change in the absorption spectra of RhB during treatment for 12 min.

Changes in the catalytic activity of sample α/γ-Fe_2O_3 in the form of kinetic curves of the RhB oxidation are shown in Figure 4a. When using the heterogeneous Fenton-like system using α/γ-Fe_2O_3 catalysts, RhB slowly decomposes and was 4% after 12-min treatment with α-Fe_2O_3. The use of UV-visible light irradiation leads to a significant acceleration of the oxidation of RhB. Irradiation with light has a dual effect on a heterogeneous system: the oxidation of the dye directly by hydrogen peroxide upon irradiation with light and the acceleration of the formation of hydroxyl radicals ($HO^{\bullet}$) as a result of the decomposition of H_2O_2 in the presence of a catalyst [78,79].

$$H_2O_2 + hv \rightarrow 2HO^{\bullet} \tag{2}$$

$$\equiv FeIII + H_2O + hv \rightarrow \equiv FeII + HO^{\bullet} + H^{+} \tag{3}$$

$$\equiv FeII + H_2O_2 \rightarrow \equiv FeIII - OH + HO^{-} \tag{4}$$

The effect of H_2O_2 concentration, catalyst dose, and RhB concentration on degradation is also shown in Figure 4. Increasing the H_2O_2 concentration improved the decomposition activity. It has been shown in the literature that only increasing the concentration of H_2O_2 up to 15 mM led to a decrease in the efficiency of decomposition due to the unfavorable consumption of excess H_2O_2 due to the effect of scavenging free radicals [80,81]. The highest performance was achieved using a catalyst dosage of 0.2 g/L. The decrease in activity with an excess of catalyst is associated with blocking the penetration of light and

active sites on the catalyst surface. A study of the effect of dye concentration on degradation efficiency (Figure 4d) demonstrated that the lower the initial concentration, the higher the efficiency. At a concentration of 1 mg/L, 99.2% of the dye decomposes in 12 min. The decrease in activity with increasing dye concentration may be due to the formation of a larger number of intermediate products that can occupy active sites on the catalyst surface. As pH is an important parameter for the photo-Fenton process, additional studies were conducted to investigate its influence. The data is presented in the Supplementary Materials (Figure S4), which show that the pH of the medium does not affect the reaction progress.

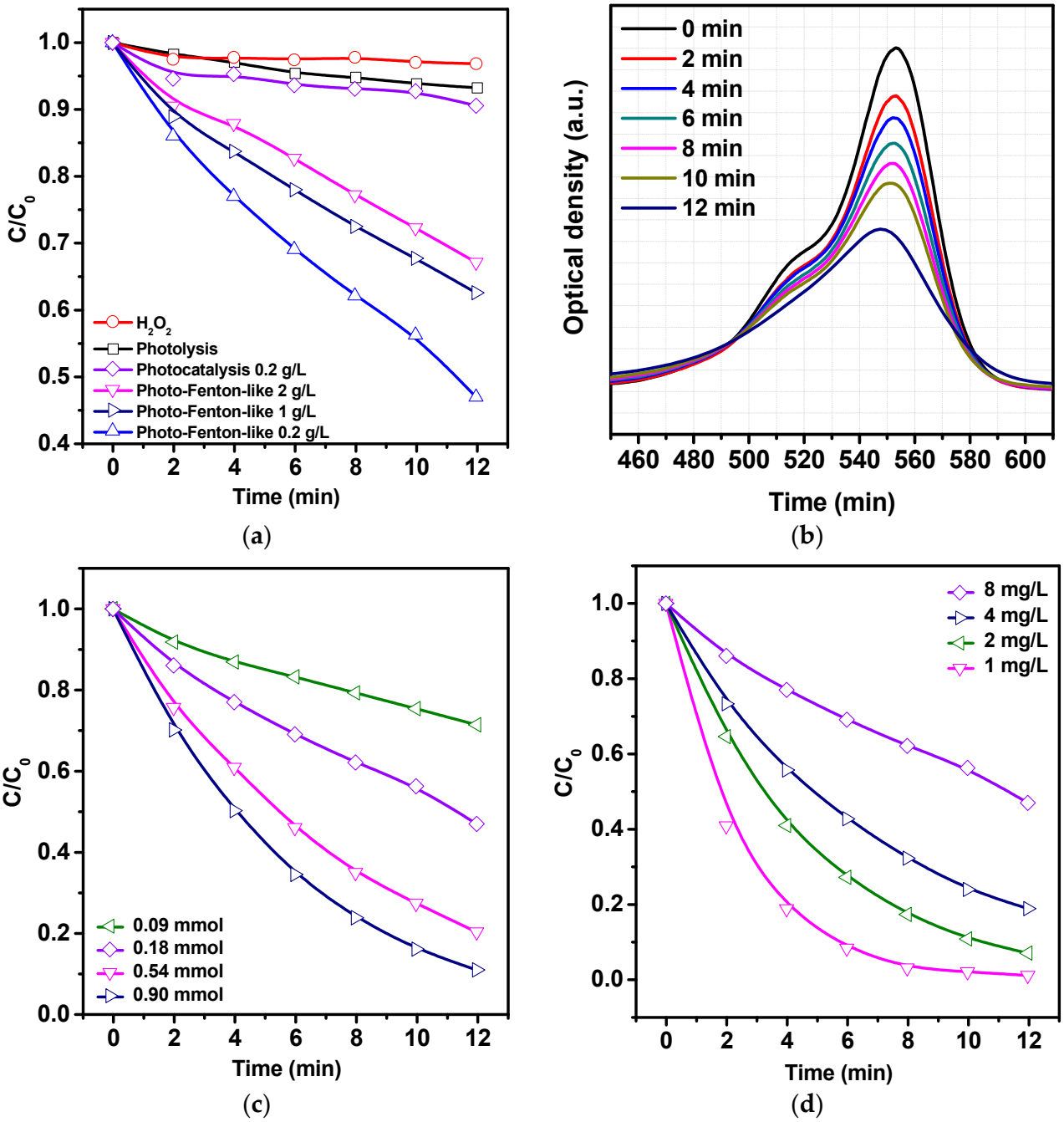

Figure 4. Kinetic curves of RhB degradation: (**a**) effect of catalyst concentration (C_{RhB} = 8 mg/L; $C(H_2O_2)$ = 0.18 mM; t =12 min), (**b**) absorption spectra of RhB during oxidation in the photo-Fenton-like process (C_{RhB} = 8 mg/L; $C(H_2O_2)$ = 0.18 mM; 0.2 g/L α/γ-Fe_2O_3; t =12 min), (**c**) H_2O_2 concentration (C_{RhB} = 8 mg/L; 0.2 g/L α/γ-Fe_2O_3; t =12 min) on the photo-Fenton-like degradation, (**d**) RhB concentration ($C(H_2O_2)$ = 0.18 mM; 0.2 g/L α/γ-Fe_2O_3; t =12 min).

Figure 5 shows the results of catalyst recycling and magnetic properties. The separation of the spent catalyst was carried out by magnetic separation. Figure 5a shows that the sample exhibits long-term stability. After five repeated uses, the activity of the catalyst decreased by 5%. However, it is also important to investigate the leaching of iron ions into the solution in the photo-Fenton-like process. After each cycle, we determined the content of iron ions in the solution using the colorimetric method with nitroso-R-salt. The results showed that the concentration of Fe^{2+} after the process was 330 μg/L.

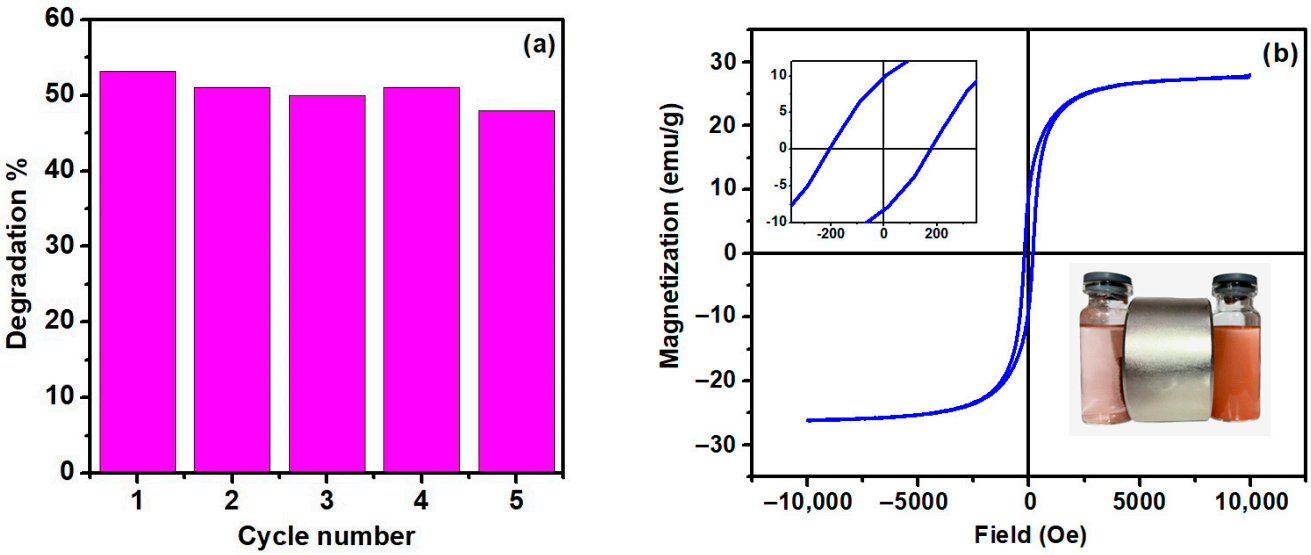

Figure 5. (**a**) Long-term catalyst stability results (C_{RhB} = 8 mg/L; $C(H_2O_2)$ = 0.18 mM; t =12 min); (**b**) magnetic hysteresis loop for mixed α/γ-Fe_2O_3.

The magnetic hysteresis loop (MH) measured at room temperature is shown in Figure 5b. The sample is ferromagnetic at room temperature.

The loop has an obvious hysteresis loop, and the coercive force (Hc) is 383.2 Oe, the magnetization vector (Ms) is 28.6 emu/g, and the remanence intensity (Mr) is 9.7 emu/g, as shown in Figure 5b. The inset to Figure 5b shows a photograph of the magnetic separation process. For clarity, a sample is presented consisting only of the α-Fe_2O_3 phase.

3. Materials and Methods

3.1. Synthesis Procedure

Synthesis of mixed α/γ-Fe_2O_3 was carried out using the combustion of glycine–nitrate precursors [59,60]. An aqueous solution of iron (III) nitrate was used as the starting material for the preparation of the two-phase α/γ-Fe_2O_3 catalyst. The precursor was prepared by mixing glycine and $Fe(NO_3)_3$ in an aqueous solution. The resulting solution was evaporated to a gel state on an electric heater with an operating temperature up to about 180 °C. During further heating, the reaction mixture ignited and iron(III) oxide powder was formed. Combustion was fast and self-sustaining, with a flame temperature of 1100 to 1450 °C. The synthesized samples were annealed at 400 °C for 1 h.

3.2. Characterizations

Characterization of the obtained heterostructures was performed using scanning electron microscopy (SEM) with the Aspex ExPress VP (FEI Company, Hillsboro, OR, USA). X-ray diffraction (XRD) studies were done using an Empyrean PANalytical X-ray diffractometer (Almelo, The Netherlands) in the radiation of a copper anode with a nickel filter, with radiation wavelength λ(CuKα) = 0.154051 nm. Data processing was performed using the High Score Plus application program, included in the instrument software, and the diffraction database ICSD (PDF-2). The surface composition was carried out by an AXIS SupraTM X-ray photoelectron spectrometer (XPS) (Kratos Analytical Ltd., Manchester, UK).

The data were processed by CasaXPS v.2.3.23 software (Casa Software Ltd., Wilmslow, UK). Raman spectra were examined by a Laser Raman 3D scanning confocal microscope (Ntegra Spectra, Moscow, Russia) using a green laser (532 nm) with a spot size of 1 μm and a resolution of 0.5 cm^{-1}.

3.3. Fenton-like Oxidation of the Rhodamine B

The catalytic activity of the samples in Fenton-like process were evaluated using the degradation of RhB in an aqueous solution (8 mg/L). The experiments were carried out in a 50 mL glass beaker. The 250 W high-pressure mercury lamp (Phillips, Amsterdam, The Netherlands) was used as a source of UV-visible light at photo-Fenton-like process investigation. The oxidant (H_2O_2) was added to the Rhodamine B solution with α/γ-Fe_2O_3 suspension. The light source was placed above the reactor at a distance of 10 cm. The RhB concentration was measured using an SF-2000 spectrophotometer (Saint-Petersburg, Russia) from the characteristic absorption peak at a wavelength of 553 nm. After the measurement, the solution was poured back into the reactor and the process continued. The concentration of iron in the solution after the process was determined by photometric method using nitroso-R-salt [82].

4. Conclusions

Heterogeneous photo-Fenton-like degradation of RhB with high efficiency has been demonstrated over a mixed-phase α/γ-Fe_2O_3 catalyst. α/γ-Fe_2O_3 was prepared by a combustion of glycine–nitrate precursors with fuel–oxidizer ratio of 0.4 ($\varphi < 1$). At the same time, a powder with a composition of 80%α/20%γ-Fe_2O_3 was synthesized, with crystal sizes of 47.4 and 45.7 nm, respectively. XPS analysis showed that Fe^{2+} ions, up to 40%, were present on the surface along with Fe^{3+} ions, due to the presence of oxygen vacancies. Optimization of photo-Fenton-like degradation of RhB showed that reducing the dye concentration from 8 to 1 mg/L, increasing the H_2O_2 concentration from 0.09 to 0.90 mmol, and reducing the mass loading from 2 to 0.2 g/L leads to an increase in catalytic activity. At optimal efficiency, 99.2% degradation is achieved in 12 min of the process. It has been shown that the pH of the medium does not affect the catalytic activity of α/γ-Fe_2O_3. The 80% α-Fe_2O_3 and 20% γ-Fe_2O_3 mixed-phase catalyst showed no obvious decrease in degradation performance over five consecutive cycles. The results show that the mixed-phase α/γ-Fe_2O_3 catalyst is a very promising catalyst that is magnetically separable and a suitable candidate for practical applications of dye containing wastewater treatment.

Supplementary Materials: The following supporting information can be downloaded at: https://www.mdpi.com/article/10.3390/catal13050872/s1, Figure S1: EDX spectra of α/γ-Fe_2O_3; Figure S2: Fe 2p level XPS spectra; Figure S3: O 1s level XPS spectra; Figure S4: Dependence of the catalytic activity of the photo-Fenton-like process on pH (C_{RhB} = 8 mg/L; C(H_2O_2) = 0.18 mM; t =12 min).

Author Contributions: Conceptualization, A.M. and A.I.; methodology, D.S., N.S.S., R.E., S.G. and N.A.; formal analysis, M.Z.; investigation, A.M., A.R., D.S., N.S.S., R.E., S.G. and N.A.; writing, A.I., F.O., R.M. and M.Z.; review and editing, A.I., M.Z. and K.K.; visualization, A.M., A.I., F.O. and R.E.; supervision, A.I. and M.Z.; project administration, A.M. and A.I.; funding acquisition, A.I., F.O. and R.M. All authors have read and agreed to the published version of the manuscript.

Funding: This research was funded by Russian Fund of Basic (RFBR) according to the research project No. 20-33-90220\20 and by the Russian Science Foundation (RSF) under project No. 22-73-10091 in part related to the synthesis of nanoparticles and XRD, Raman, XPS, VSM investigation.

Data Availability Statement: The data presented in this study are available on request from the corresponding author.

Acknowledgments: We acknowledge CzechNanoLab Research Infrastructure supported by MEYS CR (LM2023051) and FEKT-S-23-8228.

Conflicts of Interest: The authors declare no conflict of interest.

References

1. Isaev, A.B.; Magomedova, A.G. Advanced Oxidation Processes Based Emerging Technologies for Dye Wastewater Treatment. *Moscow Univ. Chem. Bull.* **2022**, *77*, 181–196. [CrossRef]
2. Boczkaj, G.; Fernandes, A. Wastewater treatment by means of advanced oxidation processes at basic pH conditions: A review. *Chem. Eng. J.* **2017**, *320*, 608–633. [CrossRef]
3. Oturan, M.A.; Aaron, J.J. Advanced oxidation processes in water/wastewater treatment: Principles and applications. A review. *Crit. Rev. Environ. Sci. Technol.* **2014**, *44*, 2577–2641. [CrossRef]
4. Pliego, G.; Zazo, J.A.; Garcia-Muñoz, P.; Munoz, M.; Casas, J.A.; Rodriguez, J.J. Trends in the Intensification of the Fenton Process for Wastewater Treatment: An Overview. *Crit. Rev. Environ. Sci. Technol.* **2015**, *45*, 2611–2692. [CrossRef]
5. Ramirez, J.H.; Maldonado-Hódar, F.J.; Pérez-Cadenas, A.F.; Moreno-Castilla, C.; Costa, C.A.; Madeira, L.M. Azo-dye Orange II degradation by heterogeneous Fenton-like reaction using carbon-Fe catalysts. *Appl. Catal. B Environ.* **2007**, *75*, 312–323. [CrossRef]
6. Palas, B.; Ersöz, G.; Atalay, S. Heterogeneous photo Fenton-like oxidation of Procion Red MX-5B using walnut shell based green catalysts. *J. Photochem. Photobiol. A Chem.* **2016**, *324*, 165–174. [CrossRef]
7. Li, X.; Li, J.; Shi, W.; Bao, J.; Yang, X. A fenton-like nanocatalyst based on easily separated magnetic nanorings for oxidation and degradation of dye pollutant. *Materials* **2020**, *13*, 332. [CrossRef]
8. Fang, Z.; Zhang, K.; Liu, J.; Fan, J.Y.; Zhao, Z.W. Fenton-like oxidation of azo dye in aqueous solution using magnetic Fe_3O_4-MnO_2 nanocomposites as catalysts. *Water Sci. Eng.* **2017**, *10*, 326–333. [CrossRef]
9. He, J.; Yang, X.; Men, B.; Wang, D. Interfacial mechanisms of heterogeneous Fenton reactions catalyzed by iron-based materials: A review. *J. Environ. Sci.* **2016**, *39*, 97–109. [CrossRef]
10. Pouran, S.R.; Abdul Aziz, A.R.; Daud, W.M.A.W. Review on the main advances in photo-Fenton oxidation system for recalcitrant wastewaters. *J. Ind. Eng. Chem.* **2015**, *21*, 53–69. [CrossRef]
11. Nishanth, T.; Dionysiou, D.D.; Pillai, S.C. Heterogeneous Fenton catalysts: A review of recent advances. *J. Hazard. Mater.* **2021**, *404*, 124082.
12. Ghasemi, E.; Ziyadi, H.; Afshar, A.M.; Sillanpää, M. Iron oxide nanofibers: A new magnetic catalyst for azo dyes degradation in aqueous solution. *Chem. Eng. J.* **2015**, *264*, 146–151. [CrossRef]
13. Baldrian, P.; Merhautová, V.; Gabriel, J.; Nerud, F.; Stopka, P.; Hrubý, M.; Beneš, M.J. Decolorization of synthetic dyes by hydrogen peroxide with heterogeneous catalysis by mixed iron oxides. *Appl. Catal. B Environ.* **2006**, *66*, 258–264. [CrossRef]
14. Isaev, A.B.; Shabanov, N.S.; Orudzhev, F.F.; Giraev, K.M.; Emirov, R.M. Electrochemical synthesis and photocatalytic properties of α-Fe_2O_3. *J. Nanosci. Nanotechnol.* **2017**, *17*, 4498–4503. [CrossRef]
15. Isaev, A.B.; Aliev, Z.M.; Adamadzieva, N.K.; Alieva, N.A.; Magomedova, G.A. The photocatalytic oxidation of azo dyes on Fe_2O_3 nanoparticles under oxygen pressure. *Nanotechnol. Russ.* **2009**, *4*, 475–479. [CrossRef]
16. Tariq, M.; Muhammad, M.; Khan, J.; Raziq, A.; Uddin, M.K.; Niaz, A.; Ahmed, S.S.; Rahim, A. Removal of Rhodamine B dye from aqueous solutions using photo-Fenton processes and novel Ni-Cu@ MWCNTs photocatalyst. *J. Mol. Liquids* **2020**, *312*, 113399. [CrossRef]
17. Zhu, X.; Zhang, L.; Zou, G.; Chen, Q.; Guo, Y.; Liang, S.; Hu, L.; North, M.; Xie, H. Carboxylcellulose hydrogel confined-Fe_3O_4 nanoparticles catalyst for Fenton-like degradation of Rhodamine B. *Int. J. Biol. Macromol.* **2021**, *180*, 792–803. [CrossRef]
18. Song, S.; Wang, Y.; Shen, H.; Zhang, J.; Mo, H.; Xie, J.; Zhou, N.-L.; Shen, J. Ultrasmall Graphene Oxide Modified with Fe_3O_4 Nanoparticles as a Fenton-Like Agent for Methylene Blue Degradation. *ACS Appl. Nano Mater.* **2019**, *2*, 7074–7084. [CrossRef]
19. Arshad, A.; Iqbal, J.; Ahmad, I.; Israr, M. Graphene/Fe_3O_4 nanocomposite: Interplay between photo-Fenton type reaction, and carbon purity for the removal of methyl orange. *Ceram. Int.* **2018**, *44*, 2643–2648. [CrossRef]
20. Chai, F.; Li, K.; Song, C.; Guo, X. Synthesis of magnetic porous Fe_3O_4/C/Cu_2O composite as an excellent photo-Fenton catalyst under neutral condition. *J. Colloid Interface Sci.* **2016**, *475*, 119–125. [CrossRef]
21. Jiang, Y.; Xie, Q.; Zhang, Y.; Geng, C.; Yu, B.; Chi, J. Preparation of magnetically separable mesoporous activated carbons from brown coal with Fe_3O_4. *Int. J. Min. Sci. Technol.* **2019**, *29*, 513–519. [CrossRef]
22. Li, Q.; Kong, H.; Li, P.; Shao, J.; He, Y. Photo-Fenton degradation of amoxicillin via magnetic TiO_2-graphene oxide-Fe_3O_4 composite with a submerged magnetic separation membrane photocatalytic reactor (SMSMPR). *J. Hazard. Mater.* **2019**, *373*, 437–446. [CrossRef]
23. Hesas, R.H.; Baei, M.S.; Rostami, H.; Gardy, J.; Hassanpour, A. An investigation on the capability of magnetically separable Fe_3O_4/mordenite zeolite for refinery oily wastewater purification. *J. Environ. Manag.* **2019**, *241*, 525–534. [CrossRef]
24. Baptisttella, A.M.; Araujo, C.M.; da Silva, M.P.; Nascimento, G.F.; Costa, G.R.; do Nascimento, B.F.; Ghislandi, M.G.; Motta Sobrinho, M.A. Magnetic Fe_3O_4-graphene oxide nanocomposite–synthesis and practical application for the heterogeneous photo-Fenton degradation of different dyes in water. *Sep. Sci. Technol.* **2021**, *56*, 425–438. [CrossRef]
25. Yin, R.; Sun, J.; Xiang, Y.; Shang, C. Recycling and reuse of rusted iron particles containing core-shell Fe-FeOOH for ibuprofen removal: Adsorption and persulfate-based advanced oxidation. *J. Clean. Prod.* **2018**, *178*, 441–448. [CrossRef]
26. Bai, Z.; Yang, Q.; Wang, J. Catalytic ozonation of sulfamethazine antibiotics using $Ce_{0.1}Fe_{0.9}OOH$: Catalyst preparation and performance. *Chemosphere* **2016**, *161*, 174–180. [CrossRef]
27. Chen, S.; Wu, Y.; Li, G.; Wu, J.; Meng, G.; Guo, X.; Liu, Z. A novel strategy for preparation of an effective and stable heterogeneous photo-Fenton catalyst for the degradation of dye. *Appl. Clay Sci.* **2017**, *136*, 103–111. [CrossRef]

28. Ribeiro, R.S.; Rodrigues, R.O.; Silva, A.M.; Tavares, P.B.; Carvalho, A.M.; Figueiredo, J.L.; Faria, J.L.; Gomes, H.T. Hybrid magnetic graphitic nanocomposites towards catalytic wet peroxide oxidation of the liquid effluent from a mechanical biological treatment plant for municipal solid waste. *Appl. Catal. B Environ.* **2017**, *219*, 645–657. [CrossRef]
29. Ma, Y.; Wang, B.; Wang, Q.; Xing, S. Facile synthesis of α-FeOOH/γ-Fe_2O_3 by a pH gradient method and the role of γ-Fe_2O_3 in H_2O_2 activation under visible light irradiation. *Chem. Eng. J.* **2018**, *354*, 75–84. [CrossRef]
30. Ai, C.; Wu, S.; Li, L.; Lei, Y.; Shao, X. Novel magnetically separable γ-Fe_2O_3/Ag/AgCl/g-C_3N_4 composite for enhanced disinfection under visible light. *Colloids Surf. A Physicochem. Eng. Asp.* **2019**, *583*, 123981. [CrossRef]
31. Wang, Y.; Fan, X.; Wang, S.; Zhang, G.; Zhang, F. Magnetically separable γ-Fe_2O_3/TiO_2 nanotubes for photodegradation of aqueous methyl orange. *Mater. Res. Bull.* **2013**, *48*, 785–789. [CrossRef]
32. Ding, M.; Chen, W.; Xu, H.; Shen, Z.; Lin, T.; Hu, K.; Lu, C.; Xie, Z. Novel A-Fe_2O_3/MXene nanocomposite as heterogeneous activator of peroxymonosulfate for the degradation of salicylic acid. *J. Hazard. Mater.* **2020**, *382*, 121064. [CrossRef] [PubMed]
33. Yang, S.; Huang, Z.; Wu, P.; Li, Y.; Dong, X.; Li, C.; Zhu, N.; Duan, X.; Dionysiou, D.D. Rapid removal of tetrabromobisphenol A by A-Fe_2O_3-x@Graphene@Montmorillonite catalyst with oxygen vacancies through peroxymonosulfate activation: Role of halogen and A-hydroxyalkyl radicals. *Appl. Catal. B Environ.* **2020**, *260*, 118129. [CrossRef]
34. Zheng, H.; Bao, J.; Huang, Y.; Xiang, L.; Faheem; Ren, B.; Du, J.; Nadagouda, M.N.; Dionysiou, D.D. Efficient degradation of atrazine with porous sulfurized Fe_2O_3 as catalyst for peroxymonosulfate activation. *Appl. Catal. B Environ.* **2019**, *259*, 118056. [CrossRef]
35. Rahim Pouran, S.; Abdul Raman, A.A.; Wan Daud, W.M.A. Review on the application of modified iron oxides as heterogeneous catalysts in Fenton reactions. *J. Clean. Prod.* **2014**, *64*, 24–35. [CrossRef]
36. Liu, Y.; Yu, C.; Dai, W.; Gao, X.; Qian, H.; Hu, Y.; Hu, X. One-pot solvothermal synthesis of multi-shelled α-Fe_2O_3 hollow spheres with enhanced visible-light photocatalytic activity. *J. Alloys Compd.* **2013**, *551*, 440–443. [CrossRef]
37. Santhosh, C.; Malathi, A.; Dhaneshvar, E.; Bhatnagar, A.; Grace, A.N.; Madhavan, J. Iron Oxide Nanomaterials for Water Purification. In *Nanoscale Materials in Water Purification*; Elsevier: Amsterdam, The Netherlands, 2019; pp. 431–446.
38. Xu, W.; Xue, W.; Huang, H.; Wang, J.; Zhong, C.; Mei, D. Morphology controlled synthesis of α-Fe_2O_{3-x} with benzimidazole-modified Fe-MOFs for enhanced photo-Fenton-like catalysis. *Appl. Catal. B Environ.* **2021**, *291*, 120129. [CrossRef]
39. Xiao, C.; Li, J.; Zhang, G. Synthesis of stable burger-like α-Fe_2O_3 catalysts: Formation mechanism and excellent photo-Fenton catalytic performance. *J. Clean. Prod.* **2018**, *180*, 550–559. [CrossRef]
40. Huang, M.; Qin, M.; Chen, P.; Jia, B.; Chen, Z.; Li, R.; Liu, Z.; Qu, X. Facile preparation of network-like porous hematite (α-Fe_2O_3) nanosheets via a novel combustion-based route. *Ceram. Int.* **2016**, *42*, 10380–10388. [CrossRef]
41. Cheng, X.L.; Jiang, J.S.; Jin, C.Y.; Lin, C.C.; Zeng, Y.; Zhang, Q.H. Cauliflower-like α-Fe_2O_3 microstructures: Toluene–water interface-assisted synthesis, characterization, and applications in wastewater treatment and visible-light photocatalysis. *Chem. Eng. J.* **2014**, *236*, 139–148. [CrossRef]
42. Khurram, R.; Wang, Z.; Ehsan, M.F. α-Fe_2O_3-based nanocomposites: Synthesis, characterization, and photocatalytic response towards wastewater treatment. *Environ. Sci. Pollut. Res.* **2021**, *28*, 17697–17711. [CrossRef] [PubMed]
43. Pang, Y.L.; Lim, S.; Ong, H.C.; Chong, W.T. Synthesis, characteristics and sonocatalytic activities of calcined γ-Fe_2O_3 and TiO_2 nanotubes/γ-Fe_2O_3 magnetic catalysts in the degradation of Orange G. *Ultrason. Sonochem.* **2016**, *29*, 317–327. [CrossRef] [PubMed]
44. Liu, Y.; Jin, W.; Zhao, Y.; Zhang, G.; Zhang, W. Enhanced catalytic degradation of methylene blue by α-Fe_2O_3/graphene oxide via heterogeneous photo-Fenton reactions. *Appl. Catal. B Environ.* **2017**, *206*, 642–652. [CrossRef]
45. Xiang, H.; Ren, G.; Yang, X.; Xu, D.; Zhang, Z.; Wang, X. A low-cost solvent-free method to synthesize α-Fe_2O_3 nanoparticles with applications to degrade methyl orange in photo-Fenton system. *Ecotoxicol. Environ. Saf.* **2020**, *200*, 110744. [CrossRef]
46. Li, M.; Zhang, C. γ-Fe_2O_3 nanoparticle-facilitated bisphenol A degradation by white rot fungus. *Sci. Bull.* **2016**, *61*, 468–472. [CrossRef]
47. Mao, G.Y.; Bu, F.X.; Wang, W.; Jiang, D.M.; Zhao, Z.J.; Zhang, Q.H.; Jiang, J.S. Synthesis and characterization of γ-Fe_2O_3/C nanocomposite as an efficient catalyst for the degradation of methylene blue. *Desalin. Water Treat.* **2016**, *57*, 9226–9236. [CrossRef]
48. Wang, F.; Yu, X.; Ge, M.; Wu, S.; Guan, J.; Tang, J.; Wu, X.; Ritchie, R.O. Facile self-assembly synthesis of γ-Fe_2O_3 /graphene oxide for enhanced photo-Fenton reaction. *Environ. Pollut.* **2019**, *248*, 229–237. [CrossRef]
49. Cao, S.; Kang, F.; Li, P.; Chen, R.; Liu, H.; Wei, Y. Photoassisted hetero-Fenton degradation mechanism of Acid Blue 74 by a γ-Fe_2O_3 catalyst. *RSC Adv.* **2015**, *5*, 66231–66238. [CrossRef]
50. Zhan, J.; Li, M.; Zhang, X.; An, Y.; Sun, W.; Peng, A.; Zhou, H. Aerosol-assisted submicron γ-Fe_2O_3/C spheres as a promising heterogeneous Fenton-like catalyst for soil and groundwater remediation: Transport, adsorption and catalytic ability. *Chin. Chem. Lett.* **2020**, *31*, 715–720. [CrossRef]
51. Rajoba, S.J.; Badabade, A.R.; Pingale, P.C.; Kale, R.D. Structural, Morphological, and Vibrational Properties of Porous α-Fe_2O_3 Nanoparticles Prepared by Combustion method. *Macromol. Symp.* **2021**, *400*, 2100033. [CrossRef]
52. Apte, S.K.; Naik, S.D.; Sonawane, R.S.; Kale, B.B.; Baeg, J.O. Synthesis of nanosize-necked structure α- and γ-Fe $_2O_3$ and its photocatalytic activity. *J. Am. Ceram. Soc.* **2007**, *90*, 412–414. [CrossRef]
53. de Andrade, M.B.; Guerra, A.C.S.; dos Santos, T.R.T.; Cusioli, L.F.; de Souza Antônio, R.; Bergamasco, R. Simplified synthesis of new GO-α-γ-Fe_2O_3-Sh adsorbent material composed of graphene oxide decorated with iron oxide nanoparticles applied for removing diuron from aqueous medium. *J. Environ. Chem. Eng.* **2020**, *8*, 103903. [CrossRef]

54. Manukyan, K.V.; Chen, Y.S.; Rouvimov, S.; Li, P.; Li, X.; Dong, S.; Liu, X.; Furdyna, J.K.; Orlov, A.O.; Bernstein, G.H.; et al. Ultrasmall α-Fe_2O_3 Superparamagnetic Nanoparticles with High Magnetization Prepared by Template-Assisted Combustion Process. *J. Phys. Chem. C* **2014**, *118*, 16264–16271. [CrossRef]
55. Tian, R.; Gao, Z.; Lang, R.; Li, N.; Gu, H.; Chen, G.; Guan, H.; Comini, E.; Dong, C. Ru-functionalized Ni-doped dual phases of α/γ-Fe_2O_3 nanosheets for an optimized acetone detection. *J. Nanostruct. Chem.* **2022**. [CrossRef]
56. Yan, S.; Zan, G.; Wu, Q. An ultrahigh-sensitivity and selective sensing material for ethanol: α-/γ-Fe_2O_3 mixed-phase mesoporous nanofibers. *Nano Res.* **2015**, *8*, 3673–3686. [CrossRef]
57. Huang, D.; Li, H.; Wang, Y.; Wang, X.; Cai, L.; Fan, W.; Chen, Y.; Wang, W.; Song, Y.; Han, G.; et al. Assembling a high-performance acetone sensor based on MOFs-derived porous bi-phase α-/γ-Fe_2O_3 nanoparticles combined with $Ti_3C_2T_x$ nanosheets. *Chem. Eng. J.* **2022**, *428*, 131377. [CrossRef]
58. Ghasemifard, M.; Heidari, G.; Ghamari, M.; Fathi, E.; Izi, M. Synthesis of Porous Network-Like α-Fe_2O_3 and α/γ-Fe_2O_3 Nanoparticles and Investigation of Their Photocatalytic Properties. *Nanotechnol. Russ.* **2019**, *14*, 353–361. [CrossRef]
59. Orudzhev, F.F.; Alikhanov, N.M.-R.; Ramazanov, S.M.; Sobola, D.S.; Murtazali, R.K.; Ismailov, E.H.; Gasimov, R.D.; Aliev, A.S.; Ţălu, Ş. Morphotropic Phase Boundary Enhanced Photocatalysis in Sm Doped $BiFeO_3$. *Molecules* **2022**, *27*, 7029. [CrossRef]
60. Alikhanov, N.M.-R.; Rabadanov, M.K.; Orudzhev, F.F.; Gadzhimagomedov, S.K.; Emirov, R.M.; Sadykov, S.A.; Kallaev, S.N.; Ramazanov, S.M.; Abdulvakhidov, K.G.; Sobola, D. Size-dependent structural parameters, optical, and magnetic properties of facile synthesized pure-phase $BiFeO_3$. *J. Mater. Sci. Mater. Electron.* **2021**, *32*, 13323–13335. [CrossRef]
61. Kashyap, S.J.; Sankannavar, R.; Madhu, G.M. Iron oxide (Fe_2O_3) synthesized via solution-combustion technique with varying fuel-to-oxidizer ratio: FT-IR, XRD, optical and dielectric characterization. *Mater. Chem. Phys.* **2022**, *286*, 126118. [CrossRef]
62. Chernyshova, I.V.; Hochella, M.F.; Madden, A.S. Size-dependent structural transformations of hematite nanoparticles. 1. Phase transition. *Phys. Chem. Chem. Phys.* **2007**, *9*, 1736–1750. [CrossRef]
63. El Mendili, Y.; Bardeau, J.F.; Randrianantoandro, N.; Gourbil, A.; Greneche, J.M.; Mercier, A.M.; Grasset, F. New evidences of in situ laser irradiation effects on γ-Fe_2O_3 nanoparticles: A Raman spectroscopic study. *J. Raman Spectrosc.* **2011**, *42*, 239–242. [CrossRef]
64. Wang, L.; Lu, X.; Han, C.; Lu, R.; Yang, S.; Song, X. Electrospun hollow cage-like α-Fe_2O_3 microspheres: Synthesis, formation mechanism, and morphology-preserved conversion to Fe nanostructures. *CrystEngComm* **2014**, *16*, 10618–10623. [CrossRef]
65. Jain, S.; Shah, J.; Negi, N.S.; Sharma, C.; Kotnala, R.K. Significance of interface barrier at electrode of hematite hydroelectric cell for generating ecopower by water splitting. *Int. J. Energy Res.* **2019**, *43*, 4743–4755. [CrossRef]
66. Jubb, A.M.; Heather, C.A. Vibrational spectroscopic characterization of hematite, maghemite, and magnetite thin films produced by vapor deposition. *ACS Appl. Mater. Interfaces* **2010**, *2*, 2804–2812. [CrossRef]
67. Bahari, A. Characteristics of Fe_3O_4, α -Fe_2O_3, and γ-Fe_2O_3 Nanoparticles as Suitable Candidates in the Field of Nanomedicine. *J. Supercond. Nov. Magn.* **2017**, *30*, 2165–2174. [CrossRef]
68. Han, Q.; Liu, Z.; Xu, Y.; Chen, Z.; Wang, T.; Zhang, H. Growth and properties of single-crystalline γ-Fe_2O_3 nanowires. *J. Phys. Chem. C* **2007**, *111*, 5034–5038. [CrossRef]
69. Zhong, Y.; Ma, Y.; Guo, Q.; Liu, J.; Wang, Y.; Yang, M.; Xia, H. Controllable Synthesis of TiO_2@Fe_2O_3 Core-Shell Nanotube Arrays with Double-Wall Coating as Superb Lithium-Ion Battery Anodes. *Sci. Rep.* **2017**, *7*, 40927. [CrossRef]
70. Sun, Y.P.; Li, X.Q.; Cao, J.; Zhang, W.X.; Wang, H.P. Characterization of zero-valent iron nanoparticles. *Adv. Colloid Interface Sci.* **2006**, *120*, 47–56. [CrossRef] [PubMed]
71. Yamashita, T.; Hayes, P. Analysis of XPS spectra of Fe^{2+} and Fe^{3+} ions in oxide materials. *Appl. Surf. Sci.* **2008**, *254*, 2441–2449. [CrossRef]
72. Zhang, C.; Liu, S.; Chen, T.; Li, Z.; Hao, J. Oxygen vacancy-engineered Fe_2O_3 nanocubes via a task-specific ionic liquid for electrocatalytic N_2 fixation. *Chem. Commun.* **2019**, *55*, 7370–7373. [CrossRef] [PubMed]
73. Pandey, J.; Sethi, A.; Uma, S.; Nagarajan, R. Catalytic Application of Oxygen Vacancies Induced by Bi^{3+} Incorporation in ThO_2 Samples Obtained by Solution Combustion Synthesis. *ACS Omega* **2018**, *3*, 7171–7181. [CrossRef] [PubMed]
74. Liang, X.; Wang, L.; Wen, T.; Liu, H.; Zhang, J.; Liu, Z.; Zhu, C.; Long, C. Mesoporous poorly crystalline α-Fe_2O_3 with abundant oxygen vacancies and acid sites for ozone decomposition. *Sci. Total Environ.* **2022**, *804*, 150161. [CrossRef] [PubMed]
75. Sang, Y.; Cao, X.; Ding, G.; Guo, Z.; Xue, Y.; Li, G.; Yu, R. Constructing oxygen vacancy-enriched Fe_2O_3@NiO heterojunctions for highly efficient electrocatalytic alkaline water splitting. *Crystengcomm* **2021**, *24*, 199–207. [CrossRef]
76. Flak, D.; Chen, Q.; Mun, B.S.; Liu, Z.; Rękas, M.; Braun, A. In situ ambient pressure XPS observation of surface chemistry and electronic structure of α-Fe_2O_3 and γ-Fe_2O_3 nanoparticles. *Appl. Surf. Sci.* **2018**, *455*, 1019–1028. [CrossRef]
77. Tian, C.M.; Li, W.W.; Lin, Y.M.; Yang, Z.Z.; Wang, L.; Du, Y.G.; Xiao, H.Y.; Qiao, L.; Zhang, J.Y.; Chen, L.; et al. Electronic Structure, Optical Properties, and Photoelectrochemical Activity of Sn-Doped Fe_2O_3Thin Films. *J. Phys. Chem. C* **2020**, *124*, 12548–12558. [CrossRef]
78. Dai, H.; Xu, S.; Chen, J.; Miao, X.; Zhu, J. Oxalate enhanced degradation of Orange II in heterogeneous UV-Fenton system catalyzed by Fe_3O_4@γ-Fe_2O_3 composite. *Chemosphere* **2018**, *199*, 147–153. [CrossRef]
79. Chen, J.; Zhu, L. UV-Fenton discolouration and mineralization of Orange II over hydroxyl-Fe-pillared bentonite. *J. Photochem. Photobiol. A Chem.* **2007**, *188*, 56–64. [CrossRef]

80. Jiang, J.; Gao, J.; Li, T.; Chen, Y.; Wu, Q.; Xie, T.; Lin, Y.; Dong, S. Visible-light-driven photo-Fenton reaction with α-Fe_2O_3/BiOI at near neutral pH: Boosted photogenerated charge separation, optimum operating parameters and mechanism insight. *J. Colloid Interface Sci.* **2019**, *554*, 531–543. [CrossRef]
81. Wang, Y.; Hongying, Z.h.a.o.; Zhao, G. Iron-copper bimetallic nanoparticles embedded within ordered mesoporous carbon as effective and stable heterogeneous Fenton catalyst for the degradation of organic contaminants. *Appl. Catal. B Environ.* **2015**, *164*, 396–406. [CrossRef]
82. Griffing, M.; Mellon, M.G. Colorimetric determination of iron with nitroso-R-salt. *Anal. Chem.* **1947**, *19*, 1014–1016. [CrossRef]